Confinement-Induced Chiral Edge Channel Interaction in Quantum Anomalous Hall Insulators

Ling-Jie Zhou,[1,*] Ruobing Mei,[1,*] Yi-Fan Zhao,[1,*] Ruoxi Zhang,[1] Deyi Zhuo,[1] Zi-Jie Yan,[1] Wei Yuan,[1] Morteza Kayyalha,[1,2] Moses H. W. Chan,[1] Chao-Xing Liu,[1,†] and Cui-Zu Chang[1,‡]

[1]*Department of Physics, Pennsylvania State University, University Park, Pennsylvania 16802, USA*

[2]*Department of Electrical Engineering, Pennsylvania State University, University Park, Pennsylvania 16802, USA*

(Received 17 July 2022; revised 20 January 2023; accepted 23 January 2023; published 21 February 2023)

In quantum anomalous Hall (QAH) insulators, the interior is insulating but electrons can travel with zero resistance along one-dimensional (1D) conducting paths known as chiral edge channels (CECs). These CECs have been predicted to be confined to the 1D edges and exponentially decay in the two-dimensional (2D) bulk. In this Letter, we present the results of a systematic study of QAH devices fashioned in a Hall bar geometry of different widths under gate voltages. At the charge neutral point, the QAH effect persists in a Hall bar device with a width of only ~72 nm, implying the intrinsic decaying length of CECs is less than ~36 nm. In the electron-doped regime, we find that the Hall resistance deviates quickly from the quantized value when the sample width is less than 1 μm. Our theoretical calculations suggest that the wave function of CEC first decays exponentially and then shows a long tail due to disorder-induced bulk states. Therefore, the deviation from the quantized Hall resistance in narrow QAH samples originates from the interaction between two opposite CECs mediated by disorder-induced bulk states in QAH insulators, consistent with our experimental observations.

DOI: 10.1103/PhysRevLett.130.086201

The search for dissipation-free electronic platforms continues to be a vibrant frontier in condensed matter physics. Two solid-state phenomena exhibit resistance-free current. One is superconductivity, which usually arises in metallic materials with high carrier density and is, thus, difficult to electrically manipulate. The other one is the chiral edge channel (CEC) formed in quantum Hall insulators [1]. The CEC can be easily switched on and off by applying a gate voltage, but the need for a high external magnetic field hampers its potential applications in electronic devices. The necessity of an external magnetic field is circumvented in the quantum anomalous Hall (QAH) effect [2–10]. The QAH insulators, like quantum Hall insulators, also possess dissipation-free CEC [2,11–15].

To date, the QAH effect has been realized in mechanically scratched [2–7,9,10,16–18] and photolithography-patterned [8,19–24] devices of Cr- and/or V-doped $(Bi, Sb)_2Te_3$ films and heterostructures. When the two CECs on opposite sides of the sample are well separated [Fig. 1(a)], the QAH effect exhibits quantized Hall resistance ρ_{yx} and zero longitudinal resistance ρ_{xx}. When the width of the QAH Hall bar w is less than $2d_0$ (d_0 is the CEC width), the two CECs are predicted to couple with each other and the QAH effect disappears [25] [Fig. 1(a)]. There is yet no reliable prediction on the value of d_0; however, for quasi-1D QAH structures with $w < 2d_0$, the helical-like conducting channels are predicted to form localized Majorana zero modes in the presence of a proximity-induced superconducting order [25,26]. This possibility and the need to miniaturize dissipation-free electronic devices provide a strong impetus to reduce the size of the QAH sample to search for the onset of interaction between neighboring CECs. The QAH effect was recently observed in

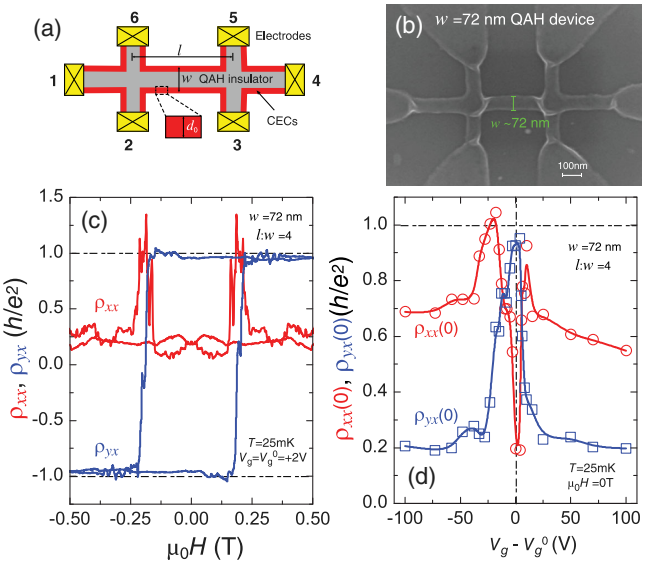

FIG. 1. The QAH state in a device with $w \sim 72$ nm. (a) Schematic of CECs. (b) The scanning electron microscope image. (c) $\mu_0 H$ dependence of ρ_{xx} (red) and ρ_{yx} (blue) measured at $V_g = V_g^0$ and $T = 25$ mK. ρ_{yx} greater than h/e^2 at certain magnetic fields might be related to the large contact resistance. (d) $(V_g\text{-}V_g^0)$ dependence of $\rho_{xx}(0)$ (red) and $\rho_{yx}(0)$ (blue) measured at $\mu_0 H = 0$ T and $T = 25$ mK.

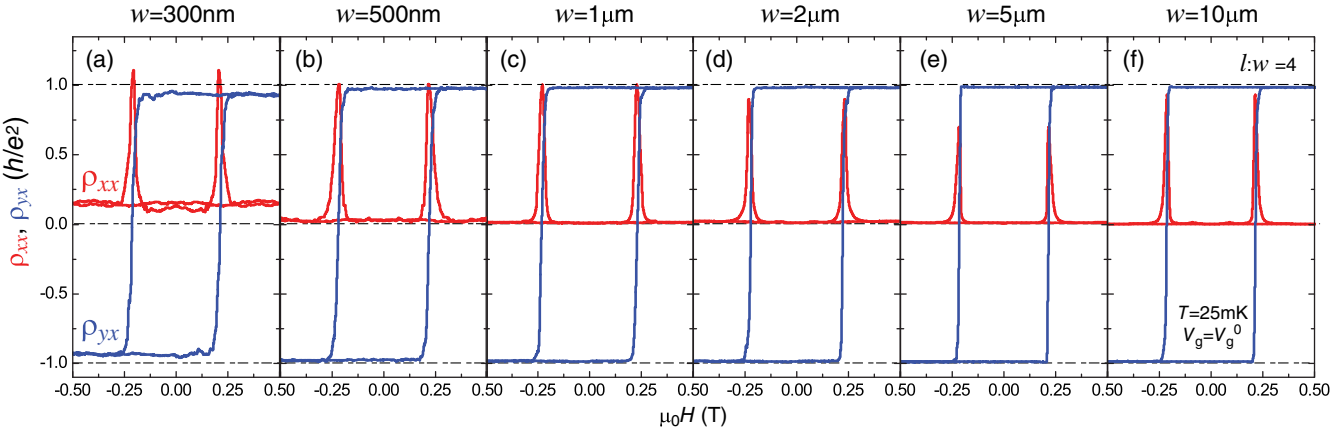

FIG. 2. The QAH state in devices with 300 nm $\leq w \leq$ 10 μm. (a)–(f) $\mu_0 H$ dependence of ρ_{xx} (red) and ρ_{yx} (blue) of the QAH devices with $w = 300$ nm (a), $w = 500$ nm (b), $w = 1$ μm (c), $w = 2$ μm (d), $w = 5$ μm (e), and $w = 10$ μm (f). All measurements are taken at $V_g = V_g^0$ and $T = 25$ mK. The values of V_g^0 are +4, +6, +8, +8, +11, and +12 V for the $w = 300$ nm, 500 nm, 1 μm, 2 μm, 5 μm, and 10 μm devices, respectively.

devices with w of ~600 nm [27] and ~160 nm [28] without showing reliable evidence of a d_0-related confinement effect.

In this Letter, we systematically search for the onset of confinement-induced CEC interaction in QAH devices with widths from 100 μm down to 72 nm from MBE-grown magnetic TI/TI sandwiches, specifically 3QL Cr-doped $(Bi, Sb)_2Te_3$/4QL $(Bi, Sb)_2Te_3$/3QL Cr-doped $(Bi, Sb)_2Te_3$ [10,29]. Our transport measurements show that the QAH state persists in a device with $w \sim 72$ nm at the charge neutral point $V_g = V_g^0$, indicating that d_0 is less than ~36 nm. This is much smaller than the value revealed in prior microscopy studies on similar QAH samples [21,30]. However, in the electron-doped regime, i.e., $V_g > V_g^0$, we find that ρ_{yx} deviates quickly from the quantized value when w is less than 1 μm. We model the decaying behaviors of CECs away from the edges and find that the density of state (DOS) of CECs comprises an exponential decay part with a short decay length and a bulklike part with a much longer localization length. Our studies suggest the deviation from the quantized Hall resistance in narrow QAH samples originates from the interaction between two CECs mediated by disorder-induced bulk states.

The QAH sandwich samples are grown on $SrTiO_3(111)$ substrates in an MBE system (Omicron Lab 10) with a vacuum better than $\sim 2 \times 10^{-10}$ mbar. The devices with 72 nm $\leq w \leq$ 10 μm are fabricated using electron-beam lithography, while the ones with 10 μm $\leq w \leq$ 100 μm are fabricated using photolithography [31]. A bottom gate voltage V_g is employed to tune the chemical potential of the QAH devices. A scanning electron microscope image of the ~72 nm device is shown in Fig. 1(b). The transport measurements are carried out by the standard lock-in amplifier technique with ~1 nA excitation current in a dilution refrigerator (Leiden Cryogenics, 10 mK, 9 T). More details of the MBE growth, device fabrication, and transport measurements can be found in Supplemental Material [31].

We first focus on the ~72 nm device. Figure 1(c) shows the magnetic field $\mu_0 H$ dependence of ρ_{xx} and ρ_{yx} measured at $V_g = V_g^0$ and $T = 25$ mK. The value of ρ_{yx} at zero magnetic field [labeled as $\rho_{yx}(0)$] is found to be $\sim 0.9517 h/e^2$ and $\rho_{xx}(0) \sim 0.1911 h/e^2$. The ratio $\rho_{yx}(0)/\rho_{xx}(0)$ corresponds to an anomalous Hall angle $\alpha \sim 78.65°$, indicating the chiral edge transport still dominates over the bulk transport; i.e., the QAH state persists in this ~72 nm device [2]. The nonzero $\rho_{xx}(0)$ is likely a signature of the confinement effect, induced by the interaction between two opposite CECs [Fig. 1(a)], which we will discuss in detail below. We note that there are fluctuations observed in ρ_{xx} and ρ_{yx}, particularly near the coercive field $\mu_0 H_c$. The fluctuations are presumably a result of the fact that w is comparable with the magnetic domain size [27,28,35,36]. The QAH state in the ~72 nm device is buttressed by the $(V_g\text{-}V_g^0)$ dependence of $\rho_{yx}(0)$ and $\rho_{xx}(0)$ [Fig. 1(d)], specifically, the nearly quantized $\rho_{yx}(0)$ peak and the sharp $\rho_{xx}(0)$ dip near $V_g = V_g^0$.

The evolution of the QAH state is demonstrated in the transport results of QAH Hall bars with 72 nm $\leq w \leq$ 100 μm. Figures 2(a)–2(f) show the $\mu_0 H$ dependence of ρ_{xx} and ρ_{yx} of the QAH devices with 300 nm $\leq w \leq$ 10 μm measured at $V_g = V_g^0$ and $T = 25$ mK. For the ~300 nm and ~500 nm devices, $\rho_{yx}(0)$ shows a nearly quantized value of $\sim 0.9545 h/e^2$ and $\sim 0.9772 h/e^2$, concomitant with $\rho_{xx}(0) \sim 0.1270 h/e^2$ and $\sim 0.0275 h/e^2$, respectively [Figs. 2(a) and 2(b)]. The QAH state steadily improves with increasing w. For the 1 μm $\leq w \leq$ 10 μm devices, $\rho_{yx}(0)$ shows a quantized value of $\sim 0.9854 h/e^2$, $\sim 0.9864 h/e^2$, $\sim 0.9880 h/e^2$, and $\sim 0.9871 h/e^2$ for $w \sim 1$, 2, 5, and 10 μm, respectively. The corresponding $\rho_{xx}(0)$ is $\sim 0.0107 h/e^2$, $\sim 0.0121 h/e^2$, $\sim 0.0093 h/e^2$, and $\sim 0.0035 h/e^2$ [Figs. 2(c)–2(f)]. The devices with 10 μm $\leq w \leq$ 100 μm and $w = 500$ μm

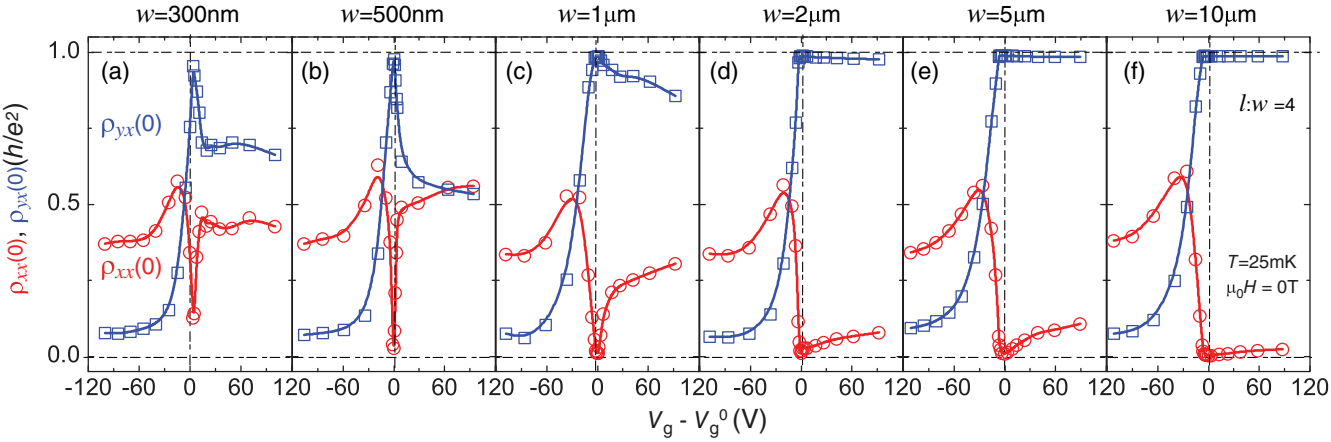

FIG. 3. Evolution of the QAH state in devices with 300 nm $\leq w \leq$ 10 μm. (a)–(f) (V_g-V_g^0) dependence of $\rho_{xx}(0)$ (red) and $\rho_{yx}(0)$ (blue) of the QAH devices with $w = 300$ nm (a), $w = 500$ nm (b), $w = 1$ μm (c), $w = 2$ μm (d), $w = 5$ μm (e), and $w = 10$ μm (f). All measurements are taken at $\mu_0 H = 0$ T and $T = 25$ mK after magnetic training. The values of $\rho_{yx}(0)$ and $\rho_{xx}(0)$ are extracted from the data point at $\mu_0 H = 0$ T.

exhibit the perfect QAH effect (Figs. S2–S4). These measurements show that, as soon as w is reduced to ~1 μm, the $\rho_{xx}(0)$ value begins to increase, while the $\rho_{yx}(0)$ value slightly drops. This behavior illustrates that confinement-induced CEC interaction starts occurring for $w \sim 1$ μm.

The QAH states in these devices are further validated by the (V_g-V_g^0) dependence of $\rho_{yx}(0)$ and $\rho_{xx}(0)$ (Figs. 3, S3, and S4). For each sample, $\rho_{yx}(0)$ exhibits a peak or plateau, demonstrating the existence of the QAH state at $V_g = V_g^0$. $\rho_{yx}(0)$ deviates slowly from h/e^2, and $\rho_{xx}(0)$ gradually increases from zero for $w \leq 1$ μm [Figs. 3(a)–3(f)]. The $\rho_{yx}(0)/\rho_{xx}(0)$ ratios correspond to anomalous Hall angles of ~82.4225°, ~88.3880°, ~89.3802°, ~89.2972°, ~89.4594°, and ~89.7986° for $w \sim 300$ nm, 500 nm, 1 μm, 2 μm, 5 μm, and 10 μm, respectively. Different decaying behaviors from the QAH state are observed for $V_g < V_g^0$ and $V_g > V_g^0$. For $V_g < V_g^0$, all QAH devices show similar (V_g-V_g^0) dependence of $\rho_{yx}(0)$ and $\rho_{xx}(0)$, i.e., deviating from the QAH state very quickly as V_g is tuned away from V_g^0 irrespective of w. For $V_g > V_g^0$, $\rho_{yx}(0)$ and $\rho_{xx}(0)$ are comparatively insensitive to V_g for devices with $w > 1$ μm. However, for $w \leq 1$ μm, by reducing w, $\rho_{yx}(0)$ and $\rho_{xx}(0)$ deviate rapidly from h/e^2 and zero, respectively, when V_g is increased from V_g^0 [Figs. 3(a)–3(f)].

We next discuss the three regimes for the decaying behavior of $\rho_{yx}(0)$. Prior studies [2,5,35,37] have demonstrated that, in QAH samples, the magnetic exchange gap Δ is close to the maximum of the bulk valence bands along the Γ-M direction but far from the bulk conduction bands [Fig. 5(f)]. For $V_g < V_g^0$, the carriers from bulk valence bands are dominant. A large number of bulk hole carriers significantly reduce $\rho_{yx}(0)$ and, thus, induce a similar (V_g-V_g^0) dependence of $\rho_{yx}(0)$ and $\rho_{xx}(0)$ behaviors. For $V_g = V_g^0$, the Coulomb disorders inevitably exist and, thus, induce charge puddles [Figs. 5(e) and S11] [31], which are expected to mediate the slow decaying behaviors [Figs. 4(a) and 4(b)]. For $V_g > V_g^0$, the disorder-induced charge puddles become larger (Fig. S11) [31] and, thus, accelerate the decaying behaviors of $\rho_{yx}(0)$ and $\rho_{xx}(0)$ (Fig. S5). In addition, the appearance of the helical surface states may further favor the confinement-induced CEC interaction for $V_g > V_g^0$ [5].

To further understand the confinement-induced CEC interaction, we plot $\rho_{yx}(0)$ and $\rho_{xx}(0)$ at $V_g = V_g^0$ and (V_g-V_g^0) = +40 V as a function of w. For $V_g = V_g^0$, we find a slow decrease in $\rho_{yx}(0)$ for $w \leq 1$ μm, accompanied by a slow increase in $\rho_{xx}(0)$ [Figs. 4(a), 4(b), and S5(a)]. However, for $V_g > V_g^0$, $\rho_{yx}(0)$ decreases and $\rho_{xx}(0)$ increases much faster for $w \leq 1$ μm [Fig. S5(b)]. We also investigate the current-induced breakdown in these QAH devices with 72 nm $\leq w \leq$ 10 μm at $V_g = V_g^0$. Since all these devices have the same aspect ratio but different lengths l, we focus on the current density-induced QAH breakdown and plot the longitudinal electric field $E_x = V_x/l$ as a function of the dc excitation current I_{dc} [V_x is the longitudinal voltage, Fig. 4(c)]. We find the nonlinear behavior in E_x-I_{dc} curves becomes more pronounced in QAH devices with smaller w, consistent with prior studies [19,20,24]. A characteristic current I_0 is defined as the horizontal intercept of the line fitted in the linear region in E_x-I_{dc} curves, which can be used to evaluate the breakdown effect. For the $w \geq 1$ μm samples, I_0 is proportional to w [Fig. 4(d)], consistent with the current-induced breakdown phenomena in micrometer-size QAH insulators [2,19,20,24]. Since the Hall electric field $E_y \sim h/e^2 \cdot I_{dc}$ increases as I_{dc} increases, our observation indicates that the current-induced breakdown in QAH devices with $w \geq$ 1 μm is relevant to E_y [20,24]. However, for the $w < 1$ μm samples, I_0 shows a sudden drop [Fig. 4(d)], which is absent in prior studies [2,19,20,24]. The current-induced QAH breakdown in this regime might be related to the confinement-induced CEC interaction, as discussed above.

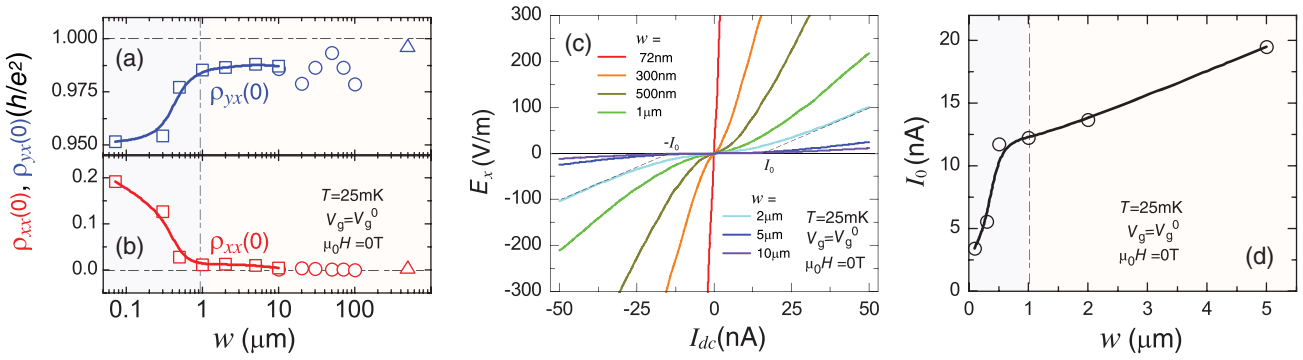

FIG. 4. Confinement-induced CEC interaction at $V_g = V_g^0$. (a),(b) w dependence of $\rho_{yx}(0)$ [blue (a)] and $\rho_{xx}(0)$ [red (b)]. The square, circle, and triangle points are from the devices fabricated by electron-beam lithography, photolithography, and mechanical scratching, respectively. (c) The longitudinal electric field E_x as a function of the dc excitation current $I_{\rm dc}$ for the QAH devices with $w \leq 10$ μm. (d) The characteristic current I_0 as a function of w.

To investigate the spatial distribution of CECs, we perform calculations using a thin-film model [10,29,38] and the recursive Green's function approach [39–41]. We choose the magnetic exchange gap $\Delta \sim 3$ meV [31], consistent with its Curie temperature $T_C \sim 17$ K (Figs. S6 and S7) [2–10,17]. We consider a slab configuration with a periodic boundary condition along the x direction and an open boundary condition along the y direction and plot the local DOS as a function of y from one to the opposite sample edge at chemical potential $\mu = 0$ meV and $\mu = 4$ meV with and without the disorder [Figs. 5(a)–5(d)]. We find two different regimes for the decaying behaviors of CECs. For $\mu = 0$ meV without disorder (i.e., $V_0 = 0$ eV), the CEC decays exponentially into the bulk with an intrinsic penetration depth $d \sim 8$ nm [Fig. 5(a)], thus supporting the good QAH effect in the ~72 nm device [Figs. 1(c) and 1(d)]. When the disorder is introduced, the CEC first decays exponentially, the same as the clean limit. However, instead of vanishing in the bulk, the CEC retains a long tail of nonzero residual DOS which extends almost as a constant into the bulk [Fig. 5(b)]. This residual DOS within Δ can mediate the interaction between two CECs, thus providing an explanation of the slow decaying behavior of the QAH state for 72 nm $\leq w \leq$ 1 μm at $V_g = V_g^0$ [Figs. 4(a) and 4(b)]. We next discuss $\mu = 4$ meV, in which the 2D conduction band states (from helical surface states) appear for both clean and disordered cases [Figs. 5(c) and 5(d)] and manifest themselves as the residual bulklike DOS that hybridize strongly with 1D CECs. Therefore, even though the intrinsic penetration depth of the CEC is short, the existence of bulklike DOS can greatly facilitate the CEC interaction [Fig. 5(e)] and, thus, accelerate the decaying behavior of $\rho_{yx}(0)$ in the electron-doped regime by narrowing the devices (Fig. S5). We note that the asymmetry between bulk conduction and valence bands [2,5,35,37] and hole carriers from bulk valence bands for $V_g < V_g^0$ have not been taken into account in our theory, so our theory applies only to the $V_g \geq V_g^0$ regime.

We next study the localization length ξ, which characterizes the propagation length of bulk states and, thus, is expected to control the slow decaying behavior of the QAH state [42,43]. Figure 5(g) shows ξ as a function of μ at different V_0. We distinguish two regimes of the QAH state. When the chemical potential crosses the 2D bulk bands

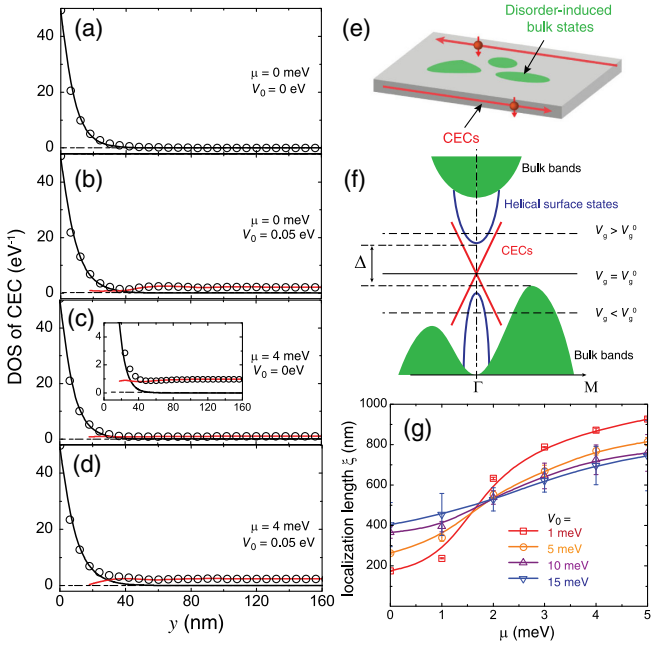

FIG. 5. Theoretical calculations of confinement-induced CEC interaction. (a)–(d) DOS of CEC as a function of the depth y at $\mu = 0$ meV and disorder strength $V_0 = 0$ eV (a), $\mu = 0$ meV and $V_0 = 0.05$ eV (b), $\mu = 4$ meV and $V_0 = 0$ eV (c), and $\mu = 4$ meV and $V_0 = 0.05$ eV (d). Inset in (c): enlarged vertical axis range to show the nonzero residual DOS caused by bulk states. (e) Schematic of CEC interaction induced by the disorder-induced bulk states. (f) The schematic band structure of the QAH sample. The two CECs (red) do not directly couple with each other, but the bulk states (green) and disorder can mediate the CEC interaction and lead to a slow deviation from the well-quantized QAH effect. (g) The localization length ξ as a function of μ at $V_0 = 1$, 5, 10, and 15 meV, respectively.

(i.e.,$|\mu| > 1.5$ meV) [Fig. 5(f)], ξ decreases with V_0, indicating that the bulk carriers are easier to localize as the disorder becomes stronger. However, when the chemical potential is located in the magnetic exchange gap (i.e., $|\mu| < 1.5$ meV), ξ increases with V_0, as expected that stronger disorders introduce more bulklike DOS within the magnetic exchange gap, and for $V_0 = 0$, the value of ξ goes toward zero, since there are no bulk states. At $\mu = 0$ meV, ξ is 200–400 nm depending on V_0, consistent with our experimental observation that the two CECs start to interact for $w \leq 1$ μm [Figs. 4(a) and 4(b)]. Therefore, by comparing our experiment and theory, we conclude the slow decaying behavior of CECs at $V_g = V_g^0$ is a result of the hybridization between two CECs mediated by the disorder-induced bulk-like states. ξ continuously increases with μ, which indicates that the QAH state deviates faster when μ is tuned away from the charge neutral point. This agrees well with our gate-dependent results (Fig. 3), where $\rho_{yx}(0)$ and $\rho_{xx}(0)$ in smaller devices deviate from the well-quantized QAH effect much faster for $V_g > V_g^0$ [Fig. S5(b)].

In summary, the confinement-induced CEC interaction starts to appear in QAH samples with $w \leq 1$ μm. The QAH state is found to persist in a device with $w \sim 72$ nm, indicating the CEC width is less than ~36 nm. We find that the current-induced QAH breakdown shows a sudden drop at the charge neutral point and the QAH effect decays much faster in the electron-doped regime by reducing the Hall bar width, both of which support the confinement-induced CEC interaction induced by disorder-induced bulk states in our QAH samples. These disorder-induced bulk states might be responsible for the bulk-dominated current in the QAH regime recently probed through electrical transport [44] and magnetic imaging [45] measurements. Our Letter lays down the dimension limitations for the QAH insulators in energy-efficient electronic and spintronic devices. The technique of patterning the quasi-1D QAH structures also enables the development of scalable topological quantum computations [2,25,26].

We are grateful to Y. T. Cui, N. Samarth, and X. D. Xu for helpful discussions. This work is primarily supported by NSF-CAREER Grant No. DMR-1847811, including sample synthesis, electron-beam lithography, and dilution transport measurements. The SEM measurements and the photolithography are supported by DOE Grant No. DE-SC0023113. The PPMS transport measurements are supported by AFOSR Grant No. FA9550-21-1-0177. C.-Z. C. acknowledges the support from Gordon and Betty Moore Foundation's EPiQS Initiative (GBMF9063 to C.-Z. C.).

*These authors contributed equally to this work.
†Corresponding author.
cxl56@psu.edu
‡Corresponding author.
cxc955@psu.edu

[1] K. von Klitzing, G. Dorda, and M. Pepper, New Method for High-Accuracy Determination of the Fine-Structure Constant Based on Quantized Hall Resistance, Phys. Rev. Lett. **45**, 494 (1980).
[2] C.-Z. Chang, C.-X. Liu, and A. H. MacDonald, Colloquium: Quantum anomalous Hall effect, Rev. Mod. Phys. **95**, 011002 (2023).
[3] C. Z. Chang *et al.*, Experimental observation of the quantum anomalous Hall effect in a magnetic topological insulator, Science **340**, 167 (2013).
[4] C. Z. Chang, W. W. Zhao, D. Y. Kim, H. J. Zhang, B. A. Assaf, D. Heiman, S. C. Zhang, C. X. Liu, M. H. W. Chan, and J. S. Moodera, High-precision realization of robust quantum anomalous Hall state in a hard ferromagnetic topological insulator, Nat. Mater. **14**, 473 (2015).
[5] C. Z. Chang, W. W. Zhao, D. Y. Kim, P. Wei, J. K. Jain, C. X. Liu, M. H. W. Chan, and J. S. Moodera, Zero-Field Dissipationless Chiral Edge Transport and the Nature of Dissipation in the Quantum Anomalous Hall State, Phys. Rev. Lett. **115**, 057206 (2015).
[6] J. G. Checkelsky, R. Yoshimi, A. Tsukazaki, K. S. Takahashi, Y. Kozuka, J. Falson, M. Kawasaki, and Y. Tokura, Trajectory of the anomalous Hall effect towards the quantized state in a ferromagnetic topological insulator, Nat. Phys. **10**, 731 (2014).
[7] X. F. Kou, S. T. Guo, Y. B. Fan, L. Pan, M. R. Lang, Y. Jiang, Q. M. Shao, T. X. Nie, K. Murata, J. S. Tang, Y. Wang, L. He, T. K. Lee, W. L. Lee, and K. L. Wang, Scale-Invariant Quantum Anomalous Hall Effect in Magnetic Topological Insulators beyond the Two-Dimensional Limit, Phys. Rev. Lett. **113**, 137201 (2014).
[8] M. Mogi, R. Yoshimi, A. Tsukazaki, K. Yasuda, Y. Kozuka, K. S. Takahashi, M. Kawasaki, and Y. Tokura, Magnetic modulation doping in topological insulators toward higher-temperature quantum anomalous Hall effect, Appl. Phys. Lett. **107**, 182401 (2015).
[9] Y. Ou, C. Liu, G. Jiang, Y. Feng, D. Zhao, W. Wu, X. X. Wang, W. Li, C. Song, L. L. Wang, W. Wang, W. Wu, Y. Wang, K. He, X. C. Ma, and Q. K. Xue, Enhancing the quantum anomalous Hall effect by magnetic codoping in a topological insulator, Adv. Mater. **30**, 1703062 (2017).
[10] Y. F. Zhao, R. Zhang, R. Mei, L. J. Zhou, H. Yi, Y. Q. Zhang, J. Yu, R. Xiao, K. Wang, N. Samarth, M. H. W. Chan, C. X. Liu, and C. Z. Chang, Tuning the Chern number in quantum anomalous Hall insulators, Nature (London) **588**, 419 (2020).
[11] C. X. Liu, S. C. Zhang, and X. L. Qi, The quantum anomalous Hall effect: Theory and experiment, Annu. Rev. Condens. Matter Phys. **7**, 301 (2016).
[12] C. Z. Chang and M. D. Li, Quantum anomalous Hall effect in time-reversal-symmetry breaking topological insulators, J. Phys. Condens. Matter **28**, 123002 (2016).
[13] H. M. Weng, R. Yu, X. Hu, X. Dai, and Z. Fang, Quantum anomalous Hall effect and related topological electronic states, Adv. Phys. **64**, 227 (2015).
[14] K. He, Y. Y. Wang, and Q. K. Xue, Topological materials: Quantum anomalous Hall system, Annu. Rev. Condens. Matter Phys. **9**, 329 (2018).
[15] Y. Tokura, K. Yasuda, and A. Tsukazaki, Magnetic topological insulators, Nat. Rev. Phys. **1**, 126 (2019).

[16] A. Kandala, A. Richardella, S. Kempinger, C. X. Liu, and N. Samarth, Giant anisotropic magnetoresistance in a quantum anomalous Hall insulator, Nat. Commun. **6**, 7434 (2015).
[17] J. Jiang, D. Xiao, F. Wang, J. H. Shin, D. Andreoli, J. X. Zhang, R. Xiao, Y. F. Zhao, M. Kayyalha, L. Zhang, K. Wang, J. D. Zang, C. X. Liu, N. Samarth, M. H. W. Chan, and C. Z. Chang, Concurrence of quantum anomalous Hall and topological Hall effects in magnetic topological insulator sandwich heterostructures, Nat. Mater. **19**, 732 (2020).
[18] C. Z. Chang, W. W. Zhao, J. Li, J. K. Jain, C. X. Liu, J. S. Moodera, and M. H. W. Chan, Observation of the Quantum Anomalous Hall Insulator to Anderson Insulator Quantum Phase Transition and its Scaling Behavior, Phys. Rev. Lett. **117**, 126802 (2016).
[19] E. J. Fox, I. T. Rosen, Y. F. Yang, G. R. Jones, R. E. Elmquist, X. F. Kou, L. Pan, K. L. Wang, and D. Goldhaber-Gordon, Part-per-million quantization and current-induced breakdown of the quantum anomalous Hall effect, Phys. Rev. B **98**, 075145 (2018).
[20] M. Kawamura, R. Yoshimi, A. Tsukazaki, K. S. Takahashi, M. Kawasaki, and Y. Tokura, Current-Driven Instability of the Quantum Anomalous Hall Effect in Ferromagnetic Topological Insulators, Phys. Rev. Lett. **119**, 016803 (2017).
[21] K. Yasuda, M. Mogi, R. Yoshimi, A. Tsukazaki, K. S. Takahashi, M. Kawasaki, F. Kagawa, and Y. Tokura, Quantized chiral edge conduction on domain walls of a magnetic topological insulator, Science **358**, 1311 (2017).
[22] S. Grauer, S. Schreyeck, M. Winnerlein, K. Brunner, C. Gould, and L. W. Molenkamp, Coincidence of superparamagnetism and perfect quantization in the quantum anomalous Hall state, Phys. Rev. B **92**, 201304(R) (2015).
[23] S. W. Wang, D. Xiao, Z. W. Dou, M. D. Cao, Y. F. Zhao, N. Samarth, C. Z. Chang, M. R. Connolly, and C. G. Smith, Demonstration of Dissipative Quasihelical Edge Transport in Quantum Anomalous Hall Insulators, Phys. Rev. Lett. **125**, 126801 (2020).
[24] G. Lippertz, A. Bliesener, A. Uday, L. M. C. Pereira, A. A. Taskin, and Y. Ando, Current-induced breakdown of the quantum anomalous Hall effect, Phys. Rev. B **106**, 045419 (2022).
[25] C. Z. Chen, Y. M. Xie, J. Liu, P. A. Lee, and K. T. Law, Quasi-one-dimensional quantum anomalous Hall systems as new platforms for scalable topological quantum computation, Phys. Rev. B **97**, 104504 (2018).
[26] Y. X. Zeng, C. Lei, G. Chaudhary, and A. H. MacDonald, Quantum anomalous Hall Majorana platform, Phys. Rev. B **97**, 081102(R) (2018).
[27] G. Qiu, P. Zhang, P. Deng, S. K. Chong, L. X. Tai, C. Eckberg, and K. L. Wang, Mesoscopic Transport of Quantum Anomalous Hall Effect in the Submicron Size Regime, Phys. Rev. Lett. **128**, 217704 (2022).
[28] K. M. Fijalkowski, N. Liu, P. Mandal, S. Schreyeck, K. Brunner, C. Gould, and L. W. Molenkamp, Macroscopic quantum tunneling of a topological ferromagnet, arXiv: 2206.03972.
[29] Y.-F. Zhao, R. Zhang, L.-J. Zhou, R. Mei, Z.-J. Yan, M. H. W. Chan, C.-X. Liu, and C.-Z. Chang, Zero Magnetic Field Plateau Phase Transition in Higher Chern Number Quantum Anomalous Hall Insulators, Phys. Rev. Lett. **128**, 216801 (2022).
[30] M. Allen, Y. T. Cui, E. Y. Ma, M. Mogi, M. Kawamura, I. C. Fulga, D. Goldhaber-Gordon, Y. Tokura, and Z. X. Shen, Visualization of an axion insulating state at the transition between 2 chiral quantum anomalous Hall states, Proc. Natl. Acad. Sci. U.S.A. **116**, 14511 (2019).
[31] See Supplemental Material at http://link.aps.org/supplemental/10.1103/PhysRevLett.130.086201 for further details regarding experimental methods, sample characterizations, more transport results, the effect of charge puddles, and more discussions, which includes Refs. [32–34].
[32] B. Skinner, Coulomb disorder in three-dimensional Dirac systems, Phys. Rev. B **90**, 060202(R) (2014).
[33] T. Knispel, W. Jolie, N. Borgwardt, J. Lux, Z. W. Wang, Y. Ando, A. Rosch, T. Michely, and M. Gruninger, Charge puddles in the bulk and on the surface of the topological insulator $BiSbTeSe_2$ studied by scanning tunneling microscopy and optical spectroscopy, Phys. Rev. B **96**, 195135 (2017).
[34] D. Nandi, B. Skinner, G. H. Lee, K. F. Huang, K. Shain, C.-Z. Chang, Y. Ou, S. P. Lee, J. Ward, J. S. Moodera, P. Kim, B. I. Halperin, and A. Yacoby, Signatures of long-range-correlated disorder in the magnetotransport of ultrathin topological insulators, Phys. Rev. B **98**, 214203 (2018).
[35] W. B. Wang, Y. B. Ou, C. Liu, Y. Y. Wang, K. He, Q. K. Xue, and W. D. Wu, Direct evidence of ferromagnetism in a quantum anomalous Hall system, Nat. Phys. **14**, 791 (2018).
[36] W. B. Wang, C. Z. Chang, J. S. Moodera, and W. D. Wu, Visualizing ferromagnetic domain behavior of magnetic topological insulator thin films, npj Quantum Mater. **1**, 16023 (2016).
[37] W. Li, M. Claassen, C. Z. Chang, B. Moritz, T. Jia, C. Zhang, S. Rebec, J. J. Lee, M. Hashimoto, D. H. Lu, R. G. Moore, J. S. Moodera, T. P. Devereaux, and Z. X. Shen, Origin of the low critical observing temperature of the quantum anomalous Hall effect in V-doped $(Bi, Sb)_2Te_3$ film, Sci. Rep. **6**, 32732 (2016).
[38] C. X. Liu, X. L. Qi, H. J. Zhang, X. Dai, Z. Fang, and S. C. Zhang, Model Hamiltonian for topological insulators, Phys. Rev. B **82**, 045122 (2010).
[39] A. Croy, R. A. Römer, and M. Schreiber, in *Parallel Algorithms and Cluster Computing* (Springer, New York, 2006), p. 203.
[40] I. Turek, V. Drchal, J. Kudrnovský, M. Sob, and P. Weinberger, *Electronic Structure of Disordered Alloys, Surfaces and Interfaces* (Springer Science & Business Media, New York, 1997).
[41] C. H. Lewenkopf and E. R. Mucciolo, The recursive Green's function method for graphene, J. Comput. Electron. **12**, 203 (2013).
[42] H. L. Li, C. Z. Chen, H. Jiang, and X. C. Xie, Coexistence of Quantum Hall and Quantum Anomalous Hall Phases in Disordered $MnBi_2Te_4$, Phys. Rev. Lett. **127**, 236402 (2021).
[43] Z. H. Qiao, Y. L. Han, L. Zhang, K. Wang, X. Z. Deng, H. Jiang, S. Y. A. Yang, J. Wang, and Q. Niu, Anderson Localization from the Berry-Curvature Interchange in Quantum Anomalous Hall Systems, Phys. Rev. Lett. **117**, 056802 (2016).

[44] I. T. Rosen, M. P. Andersen, L. K. Rodenbach, L. Tai, P. Zhang, K. L. Wang, M. A. Kastner, and D. Goldhaber-Gordon, Measured Potential Profile in a Quantum Anomalous Hall System Suggests Bulk-Dominated Current Flow, Phys. Rev. Lett. **129**, 246602 (2022).

[45] G. M. Ferguson, R. Xiao, A. R. Richardella, D. Low, N. Samarth, and K. C. Nowack, Direct visualization of electronic transport in a quantum anomalous Hall insulator, arXiv:2112.13122.